ADVANCED MATERIALS
www.advmat.de

Check for updates

Molecular Dopant-Dependent Charge Transport in Surface-Charge-Transfer-Doped Tungsten Diselenide Field Effect Transistors

Jae-Keun Kim, Kyungjune Cho, Juntae Jang, Kyeong-Yoon Baek, Jehyun Kim, Junseok Seo, Minwoo Song, Jiwon Shin, Jaeyoung Kim, Stuart S. P. Parkin, Jung-Hoon Lee, Keehoon Kang,* and Takhee Lee**

The controllability of carrier density and major carrier type of transition metal dichalcogenides(TMDCs) is critical for electronic and optoelectronic device applications. To utilize doping in TMDC devices, it is important to understand the role of dopants in charge transport properties of TMDCs. Here, the effects of molecular doping on the charge transport properties of tungsten diselenide (WSe_2) are investigated using three p-type molecular dopants, 2,3,5,6-tetrafluoro-7,7,8,8-tetracyanoquinodimethane (F_4-TCNQ), tris(4-bromophenyl) ammoniumyl hexachloroantimonate (magic blue), and molybdenum tris(1,2-bis(trifluoromethyl)ethane-1,2-dithiolene) (Mo(tfd-$COCF_3)_3$). The temperature-dependent transport measurements show that the dopant counterions on WSe_2 surface can induce Coulomb scattering in WSe_2 channel and the degree of scattering is significantly dependent on the dopant. Furthermore, the quantitative analysis revealed that the amount of charge transfer between WSe_2 and dopants is related to not only doping density, but also the contribution of each dopant ion toward Coulomb scattering. The first-principles density functional theory calculations show that the amount of charge transfer is mainly determined by intrinsic properties of the dopant molecules such as relative frontier orbital positions and their spin configurations. The authors' systematic investigation of the charge transport of doped TMDCs will be directly relevant for pursuing molecular routes for efficient and controllable doping in TMDC nanoelectronic devices.

1. Introduction

2D layered materials have attracted remarkable attention due to their ultrathin nature with thickness-dependent tunable electronic structure which make them a promising candidate for the next-generation electronic and optoelectronicdevices.[1–13] In particular, semiconducting transition metal dichalcogenides (TMDCs), such as molybdenum disulfide (MoS_2) and tungsten diselenide (WSe_2), have shown desirable field-effect transistor (FET) properties such as the high on–off ratio, high mobility, and low subthreshold swing voltage.

To utilize TMDCs for various electronic and optoelectronic device applications, the ability to control conductivity and carrier type is essential. In this manner, several studies have been reported for controlling the electrical properties of TMDCs by doping which allows tuning of free carrier concentration and the majority carrier type.[14–23] One of the approaches is substitutional doping, which is replacing transition metal elements (Mo, We) in

J.-K. Kim, J. Jang, K.-Y. Baek, J. Kim, J. Seo, M. Song, J. Shin, J. Kim, T. Lee
Department of Physics and Astronomy and Institute of Applied Physics
Seoul National University
Seoul 08826, Korea
E-mail: tlee@snu.ac.kr

J.-K. Kim, K. Cho, S. S. P. Parkin
Max-Planck Institute of Microstructure Physics
Weinberg 2, 06120 Halle (Saale), Germany

K. Cho
Soft Hybrid Materials Research Center
Korea Institute of Science and Technology
Seoul 02792, Korea

J.-H. Lee
Computational Science Research Center
Korea Institute of Science and Technology
Seoul 02792, Korea
E-mail: jhlee84@kist.re.kr

K. Kang
Department of Materials Science & Engineering
Yonsei University
Seoul 03722, Korea
E-mail: keehoon.kang@yonsei.ac.kr

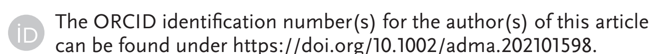
The ORCID identification number(s) for the author(s) of this article can be found under https://doi.org/10.1002/adma.202101598.

DOI: 10.1002/adma.202101598

© 2021 Wiley-VCH GmbH

TMDCs with other elements with a different number of valence electrons (such as Nb, Re, or Zr).[14–16] Although substitutional doping has an advantage in terms of the doping stability, the controllability of doping level is comparatively difficult to achieve via a direct synthesis.[15,24] Another route for controlling the electrical characteristics of TMDCs is by surface charge transfer doping (SCTD).[17–23] SCTD involves physisorption of dopants on the surface of TMDCs, which induces a charge transfer across the TMDC/dopant interface. A large surface area to volume ratio of 2D layered TMDCs makes them highly sensitive to the surface-attached dopants. In addition, comparing to substitutional doping, SCTD has an advantage that it is a relatively non-destructive process. Particularly, for SCTD by molecular reductants (oxidants) for n(p)-type doping, the potential range of material selection for dopants is diverse due to a high degree of freedom in the molecular design.[25] For these reasons, several studies have demonstrated the applicability of molecular SCTD in TMDC electronic devices for reducing contact resistance and controlling the carrier type for complementary logic applications.[19–21,26–28]

Considering that SCTD involves the creation of charged dopants on the surface of the doped TMDCs, it is natural to consider the Coulomb scattering induced by the dopants in the proximity to the charge carriers in TMDC. In this regard, in graphene, SCTD was shown to induce charged impurity scattering which significantly affected the charge transport.[29] Likewise, we can expect that SCTD will induce charged impurity scattering in doped TMDCs. Ideally, molecular SCTD should preserve the high carrier mobility of TMDCs by minimizing the charged impurity scattering.[30,31] Therefore, in order to fully realize the potential of molecular doping, it is essential to understand what fundamental properties of molecular dopants and their interfacial properties with TMDCs determine the degree of charge transfer, as well as their effects on the overall charge transport, both of which have been rarely studied. In particular, a direct relationship between local charge transfer processes of different molecular dopants and their effects on the charge transport properties of TMDC devices is yet to be quantified. Here, we systematically studied the electrical transport in doped WSe_2 by SCTD using three p-type molecular dopants with different electron affinities. Considering that doping strength of each molecular dopant is typically dependent on intrinsic molecular properties such as their relative frontier orbital positions, we investigated the doping effects on the charge transport of WSe_2 FETs by measuring the temperature-dependent intrinsic channel mobility values. Additionally, we performed first-principle density functional theory (DFT) calculations to compute and compare the degrees of charge transfer from WSe_2 to molecular dopants, which could be related to a varying degree of charged-impurity scattering induced by each dopant ion.

2. Results and Discussion

As the p-type molecular dopants for SCTD on WSe_2, three different molecules were used in this study; 2,3,5,6-tetrafluoro-7,7,8,8-tetracyanoquinodimethane (F_4-TCNQ), tris(4-bromophenyl)ammoniumyl hexachloroantimonate (magic blue), molybdenum tris(1,2-bis(trifluoromethyl)ethane-1,2-dithiolene) (Mo(tfd-$COCF_3$)$_3$). The molecular structure of each dopant is shown in **Figure 1**a. The dopants with different lowest unoccupied molecular orbital (LUMO) levels were chosen for investigating different doping strengths according to the LUMO level which correlates with the electron affinity. Figure 1b shows the energy diagrams for the valence band maximum (VBM) of WSe_2 and LUMO levels of the molecular

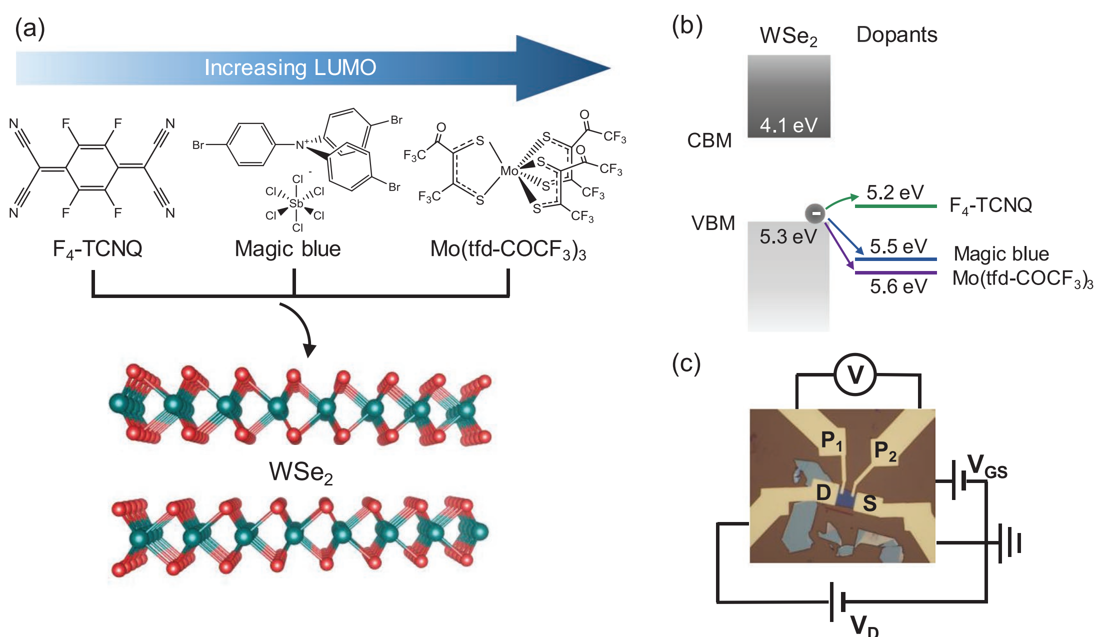

Figure 1. a) The lattice structure of WSe_2 and the molecular structures of F_4-TCNQ, magic blue, and Mo(tfd-$COCF_3$)$_3$ molecular dopants. b) Energy diagram of WSe_2 and the LUMO levels of dopant molecules. CBM and VBM are the abbreviations of conduction band minimum and valence band maximum, respectively. c) The schematic of four-point probe measurement with optical image of a WSe_2 FET.

© 2021 Wiley-VCH GmbH

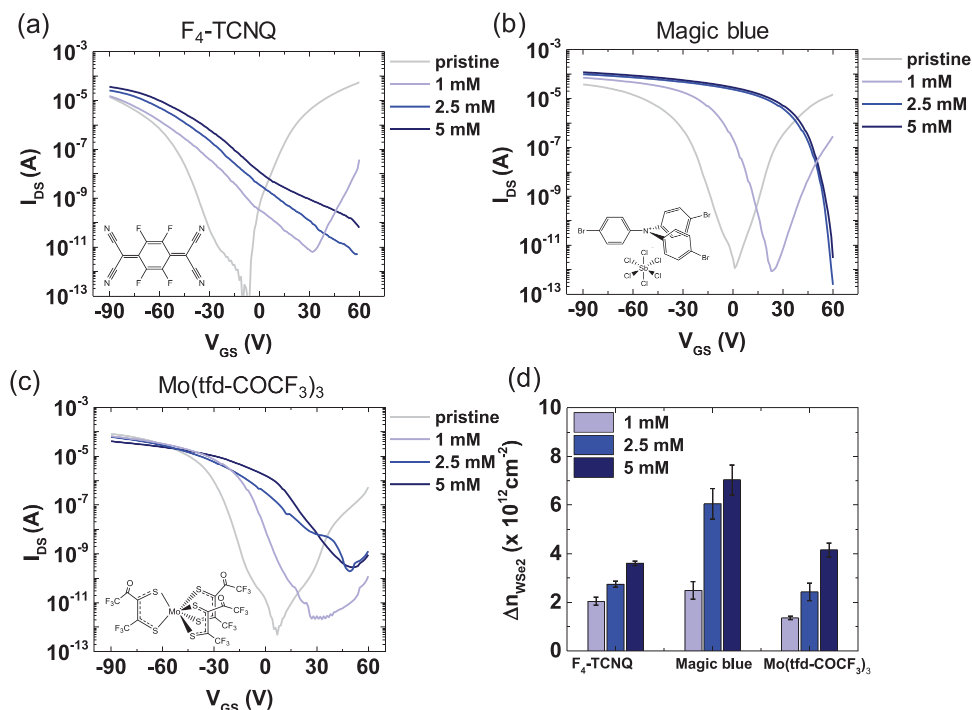

Figure 2. The representative transfer curves of pristine and p-doped WSe_2 FETs by a) F4-TCNQ, b) magic blue, and c) Mo(tfd-$COCF_3$)$_3$ with three different dopant solution concentration. d) The carrier density generated by F_4-TCNQ, magic blue, and Mo(tfd-$COCF_3$)$_3$ doping (Δn_{WSe2}) with three different dopant solution concentration. Error bars indicate the standard deviation from the mean value extracted from several devices.

dopants. Due to similar (F_4-TCNQ) or deeper (magic blue and Mo(tfd-$COCF_3$)$_3$) LUMO levels of the dopants relative to the VBM of WSe_2 (5.33 eV),[32,33] all three molecules are expected to act as p-type dopants. Also, it is expected that magic blue (LUMO level: 5.5 eV)[21] and Mo(tfd-$COCF_3$)$_3$ (5.6 eV)[34] generate a higher carrier density in WSe_2 FETs than F_4-TCNQ (5.2 eV).[35] To measure the intrinsic channel mobility of WSe_2 FETs, we employed a four-point probe measurement as schematically shown in the optical image of a WSe_2 FET device in Figure 1c. In this measurement, the intrinsic conductance of WSe_2 channel (i.e., free from contact resistance) can be obtained by measuring the voltage difference between the two inner probes (P_1, P_2) located in the channel while current was flown between the contacts (S, D) by applying drain (V_D) and gate voltages (V_{GS}). In device fabrication, we confirmed that the effect of thickness of WSe_2 on doping was not dominant in our devices (see details in Experimental Section and Supporting Information).

Before we conducted the four-point probe measurement, the effects of the molecular dopants were investigated through conventional FET measurement with two-probe measurements. **Figure 2**a–c shows representative transfer curves of pristine WSe_2 FETs and p-doped WSe_2 FETs with F_4-TCNQ, magic blue, and Mo(tfd-$COCF_3$)$_3$ at different doping levels. The pristine WSe_2 FETs exhibited typical ambipolar characteristics.[36,37] As shown in Figure 2a, for F_4-TCNQ molecular solution the threshold voltage shifts to the positive gate voltage direction, indicating the typical p-type doping behavior. As the dopant solution concentration of F_4-TCNQ increases from 1 to 5 mM, the current level of the WSe_2 FET increases and the threshold voltage shifts to the higher positive gate voltage. This result demonstrates the controllability of F_4-TCNQ doping via a sequential doping with the varying solution concentration. The same doping processes were performed for the other two molecular dopants (magic blue and Mo(tfd-$COCF_3$)$_3$) in the same manner as F_4-TCNQ. As shown in Figure 2b,c, the overall results exhibit similar characteristics for the other two dopants; the current level increases and the threshold voltage shifts to positive gate voltage direction with increasing dopant solution concentration. We can clearly see consistent results for several devices (see Figure S2, Supporting Information). Furthermore, we confirmed the p-type doping behavior by the shift of work function of WSe_2 after doping using the Kelvin probe force microscope measurement (see Figure S3, Supporting Information).

To compare the doping strength and doping range achievable with each molecular dopant, we have calculated the amount of generated carrier density by doping (Δn_{WSe2}) using the following relation $\Delta n_{WSe2} = C_i \Delta V_{th}$, where C_i is the capacitance per unit area of the bottom SiO_2 layer ($C_i = [\varepsilon_0\ \varepsilon_r]/d = 1.3 \times 10^{-4}$ F m^{-2}, where ε_o is the permittivity of vacuum [8.85×10^{-12} F m^{-1}], ε_r is dielectric constant of SiO_2 [3.9], and d is thickness of SiO_2 [270 nm]) and ΔV_{th} is the shift in the threshold voltage of the doped WSe_2 FETs relative to the pristine devices. Δn_{WSe2} for three molecular dopants cases are summarized in Figure 2d. For this figure, several WSe_2 FETs (typically four to six devices) were measured to obtain the average ΔV_{th} and standard deviation values shown as error bars. For all the three molecular dopants, Δn_{WSe2} increases with increasing the concentration of the dopant solutions, as shown in Figure 2d. It is worth noting that the maximum Δn_{WSe2} for F_4-TCNQ (3.61×10^{12} cm^{-2}) was lower than that

© 2021 Wiley-VCH GmbH

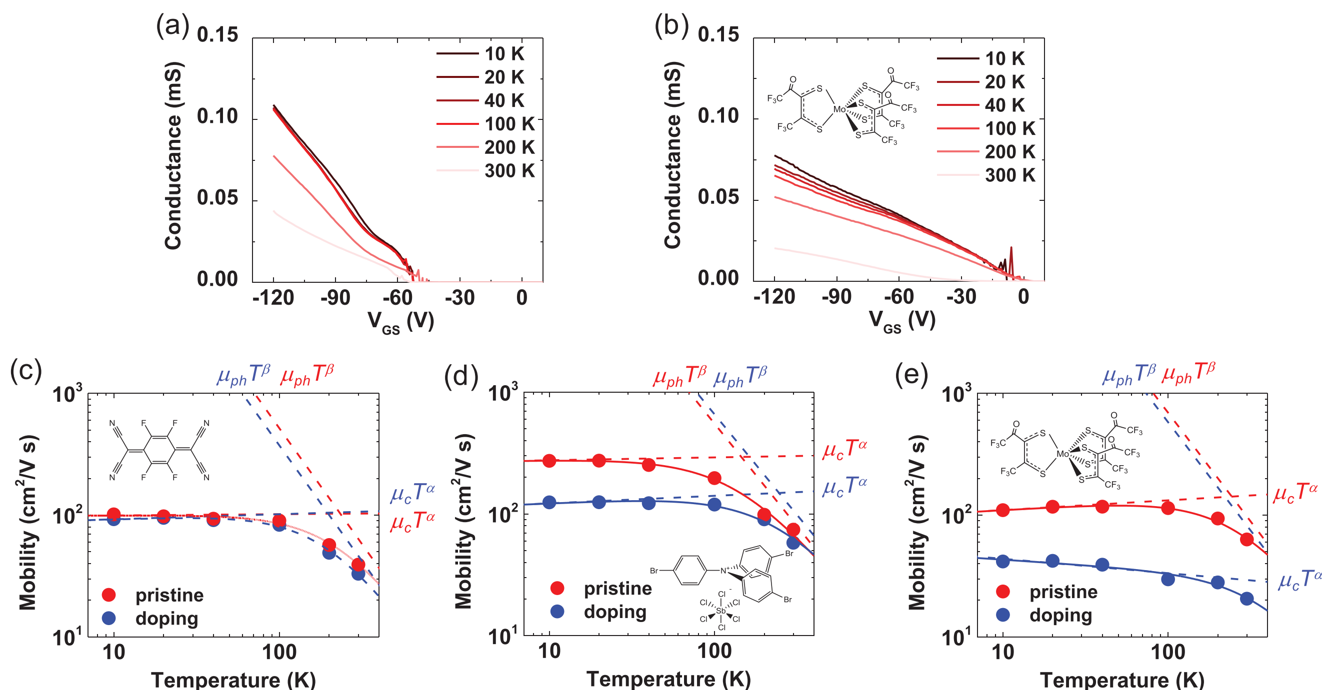

Figure 3. The representative gate-voltage dependent conductance curves of a) pristine and b) Mo(tfd-COCF$_3$)$_3$-doped WSe$_2$ devices at various temperatures. The representative temperature-dependent intrinsic mobility values extracted for the pristine and doped WSe$_2$ devices with c) F$_4$-TCNQ, d) magic blue, and e) Mo(tfd-COCF$_3$)$_3$.

for magic blue (7.03 × 10^{12} cm^{-2}) and Mo(tfd-COCF$_3$)$_3$ devices (4.15 × 10^{12} cm^{-2}). Interestingly, although the LUMO levels of magic blue and Mo(tfd-COCF$_3$)$_3$ are comparable, the maximum Δn_{WSe2} for magic blue is about 1.7 times larger than that for Mo(tfd-COCF$_3$)$_3$. This indicates that the relative LUMO level of the dopant molecules with respect to the VBM of WSe$_2$ is not the sole parameter that determines the doping strength. In other words, we need to consider both extrinsic (e.g., coverage of the dopant molecules on the surface of TMDCs[38,39]) and intrinsic factors (e.g., relative frontier orbital position) for doping. In this regards, we conducted X-ray photoelectron spectroscopy (XPS) and atomic force microscope (AFM) for investigating the surface coverage of dopant molecules (see Section S4, Supporting Information). In the surface coverage analysis with XPS and AFM, we confirmed that the dopants are not distributed uniformly on the WSe$_2$ surface but instead form grain-like structures. In addition, multilayer stacking of dopant molecules was indicated by the AFM measurements similarly to a previous report.[40] The larger coverage of magic blue dopant molecules compared to that of Mo(tfd-COCF$_3$)$_3$ can explain the higher maximum Δn_{WSe2} when doped with magic blue dopants (see Figure S4, Supporting Information).

Because both the channel resistance and contact resistance are affected after doping (Figure S6, Supporting Information), the doping effect to the channel resistance should be separated from that to the contact resistance for investigating the effect of doping to charge transport of WSe$_2$. In this study, we focus on the intrinsic mobility changes of the channel by eliminating the contribution of the contact resistance toward the total resistance of the device (see Figure 1c). Using four-point probe measurement configuration, we conducted temperature-dependent electrical characterization. **Figure 3**a,b shows typical gate-voltage dependent conductance curves of pristine and Mo(tfd-COCF$_3$)$_3$-doped WSe$_2$ devices, respectively, at different temperatures. The temperature-dependent conductance curves of the doped WSe$_2$ with the other dopants (F$_4$-TCNQ and magic blue) are provided in the Figure S7 of Supporting Information. The channel mobility can be calculated from the conductance curve by $\mu_{\mathrm{FET}} = (dG/dV_{\mathrm{GS}}) \times (L/WC_{\mathrm{i}})$, where $C_{\mathrm{i}} = 1.3 \times 10^{-4}$F m^{-2} and G, L, and W denote the conductance, the channel length, and the channel width, respectively. Figure 3c–e shows the temperature-dependent intrinsic mobility values for the pristine and doped WSe$_2$ devices with 2.5 mM solution. To investigate different scattering mechanisms in the doped WSe$_2$ devices, we decompose the temperature dependence of the mobility by using Matthienssen's rule

$$\mu_{FET}(\mathrm{T}) = \left(1/\mu_{\mathrm{C}}T^{\alpha} + 1/\mu_{\mathrm{Ph}}T^{\beta}\right)^{-1} \quad (1)$$

where T, μ_{C}, μ_{Ph}, and α and β denote temperature, charged impurity scattering-limited mobility at the zero temperature, phonon-limited mobility at the zero temperature, and their exponents, respectively. The contribution from each scattering mechanism (i.e., charged impurity scattering [$\mu_{\mathrm{C}}T^{\alpha}$] and phonon scattering [$\mu_{\mathrm{Ph}}T^{\beta}$]) are shown in Figure 3c–e as dashed lines. The values of these components are summarized in Table S5 of Supporting Information. In this analysis, we assume that the scattering from intrinsic defects in WSe$_2$ (e.g., Se vacancies[41]) and other scattering sources near the substrate were negligible in our multilayer WSe$_2$ FET devices.[42] These are relevant since the charged impurity scattering (i.e., a long-range scattering) and phonon scattering

 © 2021 Wiley-VCH GmbH

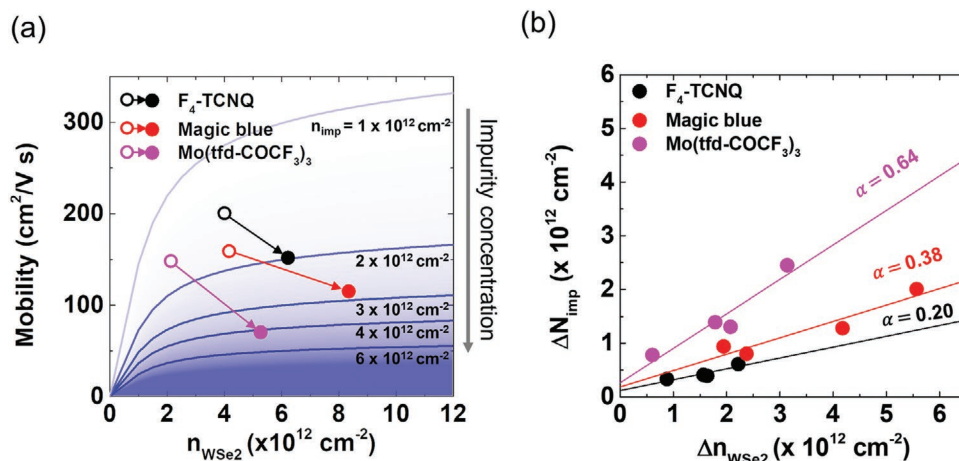

Figure 4. a) The carrier density dependent calculated WSe_2 mobility with different n_{imp} (lines) and the experimentally measured intrinsic mobility of pristine and doped WSe_2 (circles). b) The plot of n_{imp} generated in WSe_2 FETs by doping (Δn_{imp}) with F_4-TCNQ, magic blue, and Mo(tfd-$COCF_3)_3$ dopants versus generated carrier density by doping (Δn_{WSe2}).

contributions are the most dominant mechanisms in the charge transport of TMDCs.[30,41]

In the case of multilayer TMDCs, a homopolar phonon mode can be dominant among the phonon modes to determine the intrinsic mobility of TMDCs.[28] Rai et al. reported that the homopolar phonon mode of MoS_2 can be suppressed by depositing a high-k amorphous titanium suboxide on top of the MoS_2 surface, which was confirmed by decreasing of β.[43] However, β value barely changed upon doping in WSe_2 devices for all the dopants (see Figure 3c–e and Table S5, Supporting Information). This suggests that the phonon scattering contribution to the charge transport properties of the WSe_2 is almost insensitive to the presence of the dopant molecules. On the contrary, the charged impurity scattering-limited mobilities of WSe_2 ($\mu_C T^{\alpha}$ in Figure 3c–e) were generally reduced after doping for all three dopants (i.e., the charged impurity scattering increased upon doping). These results indicate that the dopant counterions created on the WSe_2 surface can act as charged impurity scattering centers for the WSe_2 channel. The mobility reduction by the externally introduced charged impurities has been well established for various semiconductor materials (e.g., Si and GaAs).[44–46] We note that the magnitude of the reduction in the charged-impurity-scattering-limited mobility (i.e., $\mu_C T^{\alpha}$) is different for each dopant, indicating that the degree of scattering in the WSe_2 channel varies with the dopant molecule.

To quantitatively analyze the degree of charged impurity scattering, we have extracted the charged impurity density present in the doped WSe_2 by relating to their transport properties. Ong et al. reported a theoretical model for calculating the charged impurity-limited mobility (μ_{imp}) of TMDCs.[31] Using this model, we obtained the charged impurity of pristine and doped WSe_2 from the intrinsic mobility value of WSe_2 at 10 K where charged impurity scattering should be the most dominant in the transport with a negligible phonon scattering. In the model, the charged impurity-limited mobility of TMDCs is determined by the scattering rate for the charged impurity scattering potential ϕ_q^{scr} for a unit charge, e. The scattering rate for the single charged impurity (Γ_{imp}) can then be given by the following equation:

$$\Gamma_{imp}(E_k) = \frac{1}{2\pi\hbar}\int d\mathbf{k}' \left|\phi^{scr}_{|\mathbf{k}-\mathbf{k}'|}\right|^2 \times (1-\cos\theta_{\mathbf{kk}'})\,\delta\left(E_{\mathbf{k}} - E_{\mathbf{k}'}\right) \tag{2}$$

where $\theta_{kk'}$ is the scattering angle between the k and k′ states. From Γ_{imp}, the charged impurity-limited mobility (μ_{imp}) is given by

$$\mu_{imp} = \frac{e}{\pi n_{WSe2}\hbar^2 k_B T}\int_0^{\infty} f(E)\left[1-f(E)\right]\left(n_{imp-doped\,(pristine)}\Gamma_{imp}(E)\right)^{-1} E dE \tag{3}$$

where $f(E)$ is the Fermi-Dirac function, k_B is the Boltzmann constant, n_{WSe2} is the carrier density, and $n_{imp\text{-}doped\ (pristine)}$ is the charged impurity density of doped (or pristine) channel. More details about the theoretical model are explained in the Supporting Information (Figure S8, Supporting Information). **Figure 4**a shows the calculated μ_{imp} from the model as a function of the carrier density in the WSe_2 channel, n_{WSe2}, for selected five different values of charged impurity density (n_{imp} = 1, 2, 3, 4, and 6 × 10^{12} cm^{-2}). To extract the experimentally determined charged impurity density for each device (N_{imp}), we compared the measured mobility values (μ_{FET}) (circles) obtained from each device to the calculated μ_{imp} values (blue lines) shown in Figure 4a. Representative mobility and carrier density (n_{WSe2}) values of the pristine (doped) WSe_2 devices obtained at V_G = −120 V are plotted as open (filled) circles in Figure 4a. A set of pristine and doped WSe_2 for each molecular dopant is denoted by different colors. As shown in Figure 4a, the mobility reduction upon doping for all three dopants, as indicated by the arrows, is a direct evidence of the Coulomb scattering induced by the dopant counterions in the doped WSe_2 devices. Therefore, we can estimate the extra impurity density generated by doping, ΔN_{imp} (= $N_{imp\text{-}doped}$ − $N_{imp\text{-}pristine}$), for each dopant from the mobility curves for various n_{imp} values as shown in Figure 4a,

© 2021 Wiley-VCH GmbH

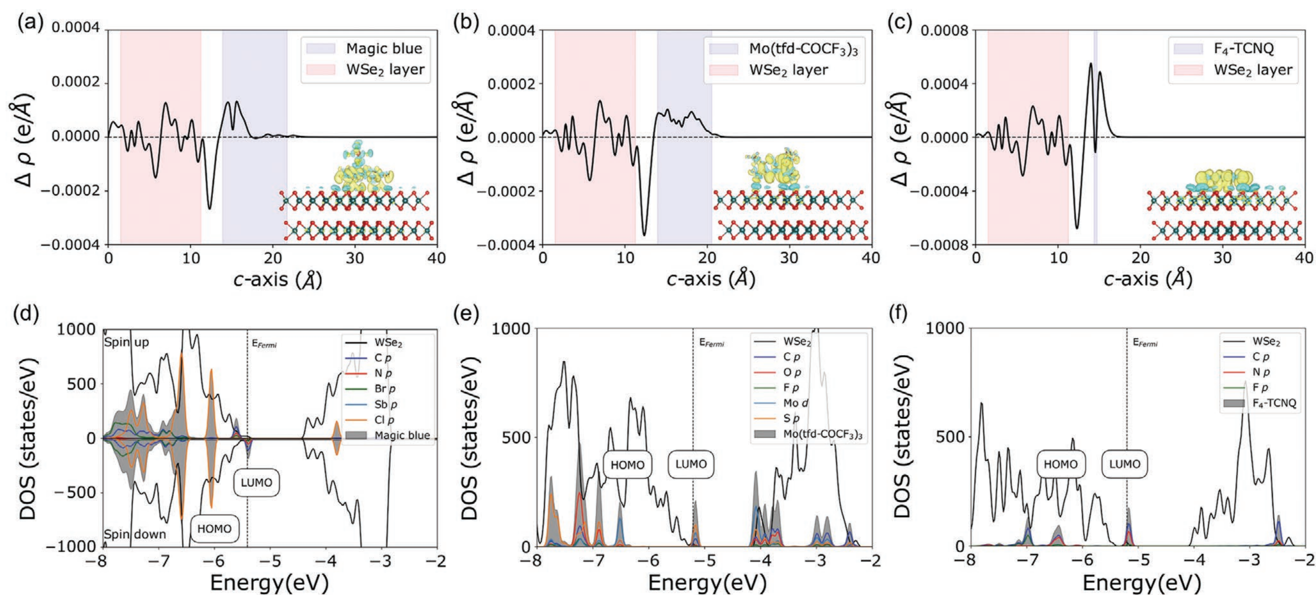

Figure 5. Computed planar-averaged charge density difference profiles along the out-of-plane for a) magic blue-, b) Mo(tfd-COCF$_3$)$_3$-, and c) F$_4$-TCNQ-doped WSe$_2$. Shaded red and blue correspond to the positions of WSe$_2$ layer and molecular dopants, respectively. Insets show isosurface plots of the charge density difference for molecular dopant binding site in WSe$_2$. Yellow and blue isosurfaces represent the excessive and deficient charge densities, respectively. The isosurface level is equal to 0.002 e Å^{-3}. Computed total and partial density of states (DOS) of d) magic blue-, e) Mo(tfd-COCF$_3$)$_3$-, and f) F$_4$-TCNQ-doped WSe$_2$. The LUMO and HOMO levels of three molecular dopants are labeled. Since the total DOS of magic blue, Mo(tfd-COCF$_3$)$_3$, and F$_4$-TCNQ are much smaller than that of the WSe$_2$ supercell, we plotted the total DOS of magic blue, Mo(tfd-COCF$_3$)$_3$, and F$_4$-TCNQ fifteen times larger than the actual values.

where $N_{\text{imp-doped}}$ and $N_{\text{imp-pristine}}$ are charged impurity density in doped and pristine WSe$_2$ devices, respectively.

The degree of Coulomb scattering induced by the dopant counterions will depend on the amount of charge transfer between WSe$_2$ and the dopant molecule. In molecular scale, the amount of charge transfer per dopant molecule (denoted as $\Delta Q = \alpha e$, where α is a constant that determines the effective degree of charge transfer) is dependent on the intrinsic molecular properties. In this case, the experimentally determined ΔN_{imp} values should not be treated as the actual charged impurity density (i.e., $\Delta n_{\text{imp}} = n_{\text{imp-doped}} - n_{\text{imp-pristine}}$, see Equation (2)) generated by doping, but should be treated as an effective charged impurity density generated by doping since the scattering potential of each dopant molecule can differ by a factor of α from a unit charge (i.e., $\Delta N_{\text{imp}} = \Delta n_{\text{imp}}$ when $\alpha = 1$). For comparing the ΔN_{imp} between dopants, we analyzed the relation between ΔN_{imp} and Δn_{WSe2} to obtain the α value of each dopant corresponding to the transferred charge (more details can be found in Section S8, Supporting Information). Considering the dopant concentration and the value of α in combination with the theoretical model, we obtain a simple relation, $\Delta N_{\text{imp}} = \alpha \Delta n_{\text{WSe2}}$. In other words, the larger the value of α, the larger the contribution of each dopant molecule toward Coulomb scattering. Figure 4b shows the ΔN_{imp} of each dopant as a function of Δn_{WSe2}, from which we found that ΔN_{imp} for Mo(tfd-COCF$_3$)$_3$ is the largest, followed by magic blue and F$_4$-TCNQ at the same doping level. That is, α value for Mo(tfd-COCF$_3$)$_3$ ($\alpha = 0.64$) is the largest, followed by magic blue (0.38) and F$_4$-TCNQ (0.20), which follows the trend of the LUMO level position of dopant molecules (Mo(tfd-COCF$_3$)$_3$ (5.6 eV) ≈ magic blue (5.5 eV) > F$_4$-TCNQ (5.2 eV)). However, the significantly lower α value of magic blue than that of Mo(tfd-COCF$_3$)$_3$ could not be explained solely by their LUMO levels. This hints toward other factors that need to be considered for predicting the α value of a dopant molecule. In addition to the Coulomb scattering, the electrical characteristics of the doped FET devices indicated the role of the dopant ions as generating trap states which are also related to the value of α (see Figure S10, Supporting Information). Thus, reducing charged impurity scattering by using a dopant with low α is desired for controlling the carrier density of WSe$_2$ while maintaining a low subthreshold swing value and high mobility.

To understand the microscopic nature of charge transfer process between WSe$_2$ and the dopant molecules, the experimentally determined values of α for each dopant can be viewed against in-depth van der Waals (vdW)-corrected DFT calculations (details on DFT calculations are provided in Supporting Information). In principle, the charge transfer process at the WSe$_2$/molecule interface is a complex problem that depends on multiple variables such as the relative frontier orbital levels, available density of states, and dielectric properties, all of which are considered in our calculations. Although our GGA level of theory is subject to slight limitations (i.e., the exact position of the frontier orbital levels and dynamic dielectric properties),[47–50] we can expect qualitative trends to be meaningful as shown in previous DFT studies[25,40,51,52] and our approaches are still relevant. From the vdW-corrected DFT calculations, we obtained the planar-averaged charge density profiles of the charge density difference $\Delta\rho = \rho_{doped-WSe_2} - (\rho_{WSe_2} + \rho_{dopant})$ along the c-axis for magic blue, Mo(tfd-COCF$_3$)$_3$, and F$_4$-TCNQ as shown in **Figure 5**a–c. Using

© 2021 Wiley-VCH GmbH

Table 1. Computed lowest unoccupied molecular orbitals (LUMOs) (in eV), the highest occupied molecular orbitals (HOMOs) (in eV), and the transferred charge per a dopant (in *e*) for WSe_2, F_4-TCNQ, magic blue, and Mo(tfd-$COCF_3$)$_3$ compared to the experiments. The reference is the vacuum level (= 0 eV).

	LUMO		HOMO		Transferred charge	
	DFT	Exp.	DFT	Exp.	DFT	Exp.
WSe_2	−3.9	—	−5.1	—	—	—
F_4-TCNQ	−6.0	−5.2	−7.3	−8.3	0.38	0.20
Magic blue	−5.9	−5.5	−6.2	—	0.24	0.38
Mo(tfd-$COCF_3$)$_3$	−5.8	−5.6	−7.1	−7.8	0.35	0.64

these profiles, we obtained the amount of charge transfer per dopant (ΔQ_{DFT}) for magic blue (0.24*e*), Mo(tfd-$COCF_3$)$_3$ (0.35*e*), and F_4-TCNQ (0.38*e*), respectively (details on the calculation in Supporting Information). We also performed layer number dependent ΔQ_{DFT} calculations and confirmed that the ΔQ_{DFT} values of each dopant tend to converge as the number of WSe_2 layers increases (see Figure S11, Supporting Information). The observed convergence could be correlated with the combined effect of available density of states in WSe_2 (which increases as the number of layers increases) and screening effect (which saturates the doping effect above a certain layer thickness). In addition, in order to validate our DFT results, we conducted the thickness dependent low-temperature measurements with different doping concentrations of magic blue dopants as a representative (see Figure S12, Supporting Information). We confirmed that the trend of the extracted α value versus the number of layers is similar to that predicted by the DFT calculations (see Figure S13, Supporting Information). In overall, our DFT calculations show an unambiguous p-type doping behavior for all the dopants and the same trend in ΔQ_{DFT} for magic blue and Mo(tfd-$COCF_3$)$_3$ as expected from αe values extracted from the experiments. The origin of the deviation of ΔQ_{DFT} from αe for F_4-TCNQ is elaborated in Section S15, Supporting Information.

We have then examined the electronic structures of three molecular dopants and doped-WSe_2 systems to elucidate the relation between the electronic structure and the charge transfer. Figure 5d–f shows the computed density of states (DOS) of WSe_2 (black line) with the dopant adsorptions (shaded black) and the partial DOS of magic blue, Mo(tfd-$COCF_3$)$_3$, and F_4-TCNQ (each atomic contribution represented in different colors). The computed DOS of the doped WSe_2 show clear evidence for p-type doping for all the dopants as shown from the downward shift in the Fermi level of WSe_2 (see Figure S14, Supporting Information for separate DOS of WSe_2 and the dopants) and partial filling of the DOS at LUMO for all the dopant molecules. More specifically, for magic blue, the DOS at LUMO level is mainly contributed by the atoms composing the tri-bromophenyl cation (C, N, and Br) which agrees well with the isosurface plot of the charge difference as visualized in the inset of Figure 5a (yellow region). In our DFT calculations, we found that the ground state of magic blue is the doublet state ($S = 1/2$) while that of the other two is the singlet state ($S = 0$). Thus, we plotted the DOS of magic blue with spin up and down components separately as shown in Figure 5d. It is worthy to note that ΔQ_{DFT} for magic blue (0.24*e*) is smaller than that of Mo(tfd-$COCF_3$)$_3$ (0.35*e*) even though the LUMO level position and the dielectric constant of magic blue are comparable to those of Mo(tfd-$COCF_3$)$_3$ (see **Table 1**) which is similar to the trend in αe values (0.38*e* for magic blue and 0.64*e* for Mo(tfd-$COCF_3$)$_3$). According to our computed DOS (Figure 5d), the reduced spin degree of freedom in charge-transfer[53] from WSe_2 to magic blue can be the origin of the smaller value of ΔQ_{DFT} of magic blue. Our computed DOS results clearly show the selective transfer of spin-down electrons from WSe_2 to the LUMO of magic blue. In overall, our DFT calculation implies that spin configuration as well as the intrinsic frontier orbital positions and dielectric constants of molecules play a significant role in determining the amount of charge transfer between WSe_2 and dopants, which broadens the scope of molecular properties that need to be considered for predicting the charge transfer effect. In addition to the well-established energetic role of frontier orbital position of dopants, we found that the other factors, such as spin configuration and dielectric constant of molecules, should also be considered to predict the charge transfer effect. Our study provides some key insights toward understanding the microscopic doping phenomenon and directly relating this to macroscopic device studies.

3. Conclusion

In conclusion, we explored dopant dependent charge transport of molecular-doped WSe_2 FETs for three different dopants via experimental determination of the intrinsic mobility values of the doped WSe_2 channels. The reduction in the intrinsic mobility after doping could be interpreted as the creation of charged impurities in the form of dopant counterions on the WSe_2 surface. Comparison between the three dopants showed that the larger the degree of charge transfer between WSe_2 and dopants, the larger the carrier density generated in WSe_2, but also the larger the degree of Coulomb scattering induced by each dopant counterion. An agreement with DFT calculations corroborated the importance of considering the selective spin transfer as well as the relative frontier orbital positions of the dopant molecules. Our results will pave the way for controlling the carrier density and conductivity levels of TMDC through molecular doping and provide criteria for selecting appropriate molecular dopants for doping applications in TMDC nanoelectronic devices such as carrier-type control of the active channel and contact doping for low-power operation.

© 2021 Wiley-VCH GmbH

4. Experimental Section

Fabrication and Electrical Characterization of Tungsten Diselenide Field-Effect Transistor Devices: WSe_2 was mechanically exfoliated from a bulk WSe_2 crystal and transferred to SiO_2/p++ Si substrate. The suitable WSe_2 flakes were founded using an optical microscope and the thickness of the flakes was measured by an AFM system (NX 10 AFM, Park Systems). After double electron resist layers, methyl methacrylate/poly(methyl methacrylate), were spin-coated, the source–drain electrodes patterns were made by using an electron-beam lithography system (JSM-6510, JEOL). Subsequently, Ti (2 nm)/Pd (40 nm)/Au (20 nm) layers were deposited by using an electron-beam evaporator (KVE-2004L, Korea Vacuum Tech.). Here, Pd was used to enhance hole injection and p-type conduction of WSe_2 FET due to its high work function (≈5.6 eV). And, Ti was used for the adhesive layer to SiO_2 and Au was used for compatibility with wire bonding. The fabricated WSe_2 FET devices were annealed at 200 °C for 1 h before the electrical measurement. The electrical characteristics of the WSe_2 FETs were measured through a semiconductor parameter analyzer (Keithley 4200-SCS) and a cryostat system (CS204*I-FMX-12, Advanced Research Systems). In device fabrication, WSe_2 flakes with a layer thickness from 6 to 15 nm were used, confirmed by AFM. In this thickness range, the substrate effect could be minimized due to a larger thickness relative to the expected screening length of WSe_2.[54] Also, it was confirmed that the effect of the thickness of WSe_2 on doping was not dominant in this thickness range (see Figures S1 and S9 and Table S5, Supporting Information).

Doping Treatment: To make a doping solution, F_4-TCNQ and Mo(tdf-$COCF_3)_3$ were dissolved in butyl acetate and magic blue was dissolved in dichloromethane. About 20 µL of the molecular dopant solution was used in a drop-casting process for each dopant.

Supporting Information

Supporting Information is available from the Wiley Online Library or from the author.

Acknowledgements

J.-K.K. and K.C. contributed equally to this work. The authors appreciate the financial support of the National Research Foundation of Korea (NRF) grant (Nos. 2021R1A2C3004783 and NRF-2021R1C1C1010266) and the Nano Material Technology Development Program grant (No. 2021M3H4A1A02049651) through NRF funded by the Ministry of Science and ICT (MSIT) of Korea. K.C. appreciates the financail support of the NRF grant funded by the Korea government (MSIT) (No. 2021R1C1C2091728). J.-H.L.'s work was supported by the KIST Institutional Program (Project No. 2E31201). Computational resources provided by KISTI Supercomputing Centre (Project No. KSC-2020-CRE-0189) are gratefully acknowledged.

Conflict of Interest

The authors declare no conflict of interest.

Data Availability Statement

Research data are not shared.

Keywords

charged impurity scattering, density functional theory, field effect transistors, surface charge transfer doping, tungsten diselenide

Received: February 26, 2021
Revised: August 15, 2021
Published online: September 17, 2021

[1] H. Li, J.-K. Huang, Y. Shi, L.-J. Li, *Adv. Mater. Interfaces* **2019**, *6*, 1900220.
[2] M. Chhowalla, D. Jena, H. Zhang, *Nat. Rev. Mater.* **2016**, *1*, 16052.
[3] B. Liu, A. Abbas, C. Zhou, *Adv. Electron. Mater.* **2017**, *3*, 1700045.
[4] K. Cho, J. Pak, S. Chung, T. Lee, *ACS Nano* **2019**, *13*, 9713.
[5] A. Nourbakhsh, A. Zubair, R. N. Sajjad, A. Tavakkoli K G, W. Chen, S. Fang, X. Ling, J. Kong, M. S. Dresselhaus, E. Kaxiras, K. K. Berggren, D. Antoniadis, T. Palacios, *Nano Lett.* **2016**, *16*, 7798.
[6] S. B. Desai, S. R. Madhvapathy, A. B. Sachid, J. P. Llinas, Q. Wang, G. H. Ahn, G. Pitner, M. J. Kim, J. Bokor, C. Hu, H.-S. P. Wong, A. Javey, *Science* **2016**, *354*, 99.
[7] G. M. Marega, Y. Zhao, A. Avsar, Z. Wang, M. Tripathi, A. Radenovic, A. Kis, *Nature* **2020**, *587*, 72.
[8] D. Y. Qiu, F. H. da Jornada, S. G. Louie, *Phys. Rev. Lett.* **2013**, *111*, 216805.
[9] D. Y. Qiu, F. H. da Jornada, S. G. Louie, *Phys. Rev. B* **2016**, *93*, 235435.
[10] H.-S. Lee, V. K. Sangwan, W. A. G. Rojas, H. Bergeron, H. Y. Jeong, J. Yuan, K. Su, M. C. Hersam, *Adv. Funct. Mater.* **2020**, *30*, 2003683.
[11] A. B. Sachid, M. Tosun, S. B. Desai, C.-Y. Hsu, D.-H. Lien, S. R. Madhvapathy, Y.-Z. Chen, M. Hettick, J. S. Kang, Y. Zeng, J.-H. He, E. Y. Chang, Y.-L. Chueh, A. Javey, C. Hu, *Adv. Mater.* **2016**, *28*, 2547.
[12] A. Avsar, K. Marinov, E. G. Marin, G. Iannaccone, K. Watanabe, T. Taniguchi, G. Fiori, A. Kis, *Adv. Mater.* **2018**, *30*, 1707200.
[13] Q. Liang, Q. Wang, Q. Zhang, J. Wei, S. X. Lim, R. Zhu, J. Hu, W. Wei, C. Lee, C. Sow, W. Zhang, A. T. S. Wee, *Adv. Mater.* **2019**, *31*, 1807609.
[14] T. Zhang, K. Fujisawa, F. Zhang, M. Liu, M. C. Lucking, R. N. Gontijo, Y. Lei, H. Liu, K. Crust, T. Granzier-Nakajima, H. Terrones, A. L. Elías, M. Terrones, *ACS Nano* **2020**, *14*, 4326.
[15] H. Gao, J. Suh, M. C. Cao, A. Y. Joe, F. Mujid, K.-H. Lee, S. Xie, P. Poddar, J.-U. Lee, K. Kang, P. Kim, D. A. Muller, J. Park, *Nano Lett.* **2020**, *20*, 4095.
[16] S. K. Pandey, H. Alsalman, J. G. Azadani, N. Izquierdo, T. Low, S. A. Campbell, *Nanoscale* **2018**, *10*, 21374.
[17] D. Kiriya, M. Tosun, P. Zhao, J. S. Kang, A. Javey, *J. Am. Chem. Soc.* **2014**, *136*, 7853.
[18] H. Fang, M. Tosun, G. Seol, T. C. Chang, K. Takei, J. Guo, A. Javey, *Nano Lett.* **2013**, *13*, 1991.
[19] D.-H. Kang, J. Shim, S. K. Jang, J. Jeon, M. H. Jeon, G. Y. Yeom, W.-S. Jung, Y. H. Jang, S. Lee, J.-H. Park, *ACS Nano* **2015**, *9*, 1099.
[20] M.-Y. Tsai, S. Zhang, P. M. Campbell, R. R. Dasari, X. Ba, A. Tarasov, S. Graham, S. Barlow, S. R. Marder, E. M. Vogel, *Chem. Mater.* **2017**, *29*, 7296.
[21] S. Zhang, H. M. Hill, K. Moudgil, C. A. Richter, A. R. H. Walker, S. Barlow, S. R. Marder, C. A. Hacker, S. J. Pookpanratana, *Adv. Mater.* **2018**, *30*, 1802991.
[22] W. Chen, S. Chen, D. Qi, X. Gao, A. Wee, *J. Am. Chem. Soc.* **2007**, *129*, 10418.
[23] W. Chen, D. Qi, X. Gao, A. Wee, *Prog. Surf. Sci.* **2009**, *84*, 279.
[24] Y. Zhao, K. Xu, F. Pan, C. Zhou, F. Zhou, Y. Chai, *Adv. Funct. Mater.* **2017**, *27*, 1603484.
[25] M. Gobbi, E. Orgiu, P. Samorì, *Adv. Mater.* **2018**, *30*, 1706103.
[26] J. Wang, Z. Ji, G. Yang, X. Chuai, F. Liu, Z. Zhou, C. Lu, W. Wei, X. Shi, J. Niu, L. Wang, H. Wang, J. Chen, N. Lu, C. Jiang, L. Li, M. Liu, *Adv. Funct. Mater.* **2018**, *28*, 1806244.
[27] L. Yu, A. Zubair, E. J. G. Santos, X. Zhang, Y. Lin, Y. Zhang, T. Palacios, *Nano Lett.* **2015**, *15*, 4928.

 © 2021 Wiley-VCH GmbH

[28] H. G. Ji, P. Solís-Fernández, D. Yoshimura, M. Maruyama, T. Endo, Y. Miyata, S. Okada, H. Ago, *Adv. Mater.* **2019**, *31*, 1903613.
[29] F. Schedin, A. K. Geim, S. V. Morozov, E. W. Hill, P. Blake, M. I. Katsnelson, K. S. Novoselov, *Nat. Mater.* **2007**, *6*, 652.
[30] N. Ma, D. Jena, *Phys. Rev. X* **2014**, *4*, 011043.
[31] Z.-Y. Ong, M. V. Fischetti, *Phys. Rev. B* **2013**, *88*, 165316.
[32] C. M. Smyth, R. Addou, S. McDonnell, C. L. Hinkle, R. M. Wallace, *2D Mater.* **2017**, *4*, 025084.
[33] F. A. Rasmussen, K. S. Thygesen, *J. Phys. Chem. C* **2015**, *119*, 13169.
[34] S. A. Paniagua, J. Baltazar, H. Sojoudi, S. K. Mohapatra, S. Zhang, C. L. Henderson, S. Graham, S. Barlow, S. R. Marder, *Mater. Horiz.* **2014**, *1*, 111.
[35] K. Kang, S. Watanabe, K. Broch, A. Sepe, A. Brown, I. Nasrallah, M. Nikolka, Z. Fei, M. Heeney, D. Matsumoto, K. Marumoto, H. Tanaka, S.-i. Kuroda, H. Sirringhaus, *Nat. Mater.* **2016**, *15*, 896.
[36] Z. Wang, Q. Li, Y. Chen, B. Cui, Y. Li, F. Besenbacher, M. Dong, *NPG Asia Mater* **2018**, *10*, 703.
[37] A. Allain, A. Kis, *ACS Nano* **2014**, *8*, 7180.
[38] Y. L. Huang, Y. J. Zheng, Z. Song, D. Chi, A. T. S. Wee, S. Y. Quek, *Chem. Soc. Rev.* **2018**, *47*, 3241.
[39] Z. Song, Q. Wang, M.-Y. Li, L.-J. Li, Y. J. Zheng, Z. Wang, T. Lin, D. Chi, Z. Ding, Y. L. Huang, A. T. S. Wee, *Phys. Rev. B* **2018**, *97*, 134102.
[40] M. Yarali, Y. Zhong, S. N. Reed, J. Wang, K. A. Ulman, D. J. Charboneau, J. B. Curley, D. J. Hynek, J. V. Pondick, S. Yazdani, N. Hazari, S. Y. Quek, H. Wang, J. J. Cha, *Adv. Electron. Mater.* **2021**, *7*, 2000873.
[41] X. Cui, G.-H. Lee, Y. D. Kim, G. Arefe, P. Y. Huang, C.-H. Lee, D. A. Chenet, X. Zhang, L. Wang, F. Ye, F. Pizzocchero, B. S. Jessen, K. Watanabe, T. Taniguchi, D. A. Muller, T. Low, P. Kim, J. Hone, *Nat. Nanotechnol.* **2015**, *10*, 534.
[42] M.-K. Joo, B. H. Moon, H. Ji, G. H. Han, H. Kim, G. Lee, S. C. Lim, D. Suh, Y. H. Lee, *Nano Lett.* **2016**, *16*, 6383.
[43] A. Rai, A. Valsaraj, H. C. P. Movva, A. Roy, R. Ghosh, S. Sonde, S. Kang, J. Chang, T. Trivedi, R. Dey, S. Guchhait, S. Larentis, L. F. Register, E. Tutuc, S. K. Banerjee, *Nano Lett.* **2015**, *15*, 4329.
[44] H. Ehrenreich, *Phys. Rev.* **1960**, *120*, 1951.
[45] A. Gold, *Appl. Phys. Lett.* **2010**, *96*, 242111.
[46] M. P. Persson, H. Mera, Y.-M. Niquet, C. Delerue, M. Diarra, *Phys. Rev. B* **2010**, *82*, 115318.
[47] J. P. Perdew, A. Zunger, *Phys. Rev. B* **1981**, *23*, 5048.
[48] J. P. Perdew, R. G. Parr, M. Levy, J. L. Balduz Jr., *Phys. Rev. Lett.* **1982**, *49*, 1691.
[49] J. P. Perdew, M. Levy, *Phys. Rev. Lett.* **1983**, *51*, 1884.
[50] L. J. Sham, M. Schlüter, *Phys. Rev. Lett.* **1983**, *51*, 1888.
[51] A. Kumar, K. Banerjee, M. Dvorak, F. Schulz, A. Harju, P. Rinke, P. Liljeroth, *ACS Nano* **2017**, *11*, 4960.
[52] H.-Z. Tsai, A. A. Omrani, S. Coh, H. Oh, S. Wickenburg, Y.-W. Son, D. Wong, A. Riss, H. S. Jung, G. D. Nguyen, G. F. Rodgers, A. S. Aikawa, T. Taniguchi, K. Watanabe, A. Zettl, S. G. Louie, J. Lu, M. L. Cohen, M. F. Crommie, *ACS Nano* **2015**, *9*, 12168.
[53] T. R. Kafle, B. Kattel, S. D. Lane, T. Wang, H. Zhao, W.-L. Chan, *ACS Nano* **2017**, *11*, 10184.
[54] V. K. Sangwan, M. C. Hersam, *Annu. Rev. Phys. Chem.* **2018**, *69*, 299.

© 2021 Wiley-VCH GmbH